Azacalixphyrin nanostructures

Daniel Ferry, Sabrina Pricl, Domenico Marson, Zhongrui Chen, Gabriel Canard, Simon Pascal, Aura Tintaru, Olivier Siri

To cite this version:

Daniel Ferry, Sabrina Pricl, Domenico Marson, Zhongrui Chen, Gabriel Canard, et al.. Azacalixphyrin nanostructures. Journal of Porphyrins and Phthalocyanines, In press, 10.1142/S1088424623500785 . hal-04046963

Azacalixphyrin nanostructures

Daniel Ferry[a], Sabrina Pricl[b,c*], Domenico Marson[b], Zhongrui Chen[a], Gabriel Canard[a], Simon Pascal[a], Aura Tintaru[a] and Olivier Siri[a*]

[a] *Aix Marseille Univ, CNRS UMR 7325, Centre Interdisciplinaire de Nanosciences de Marseille (CINaM), Campus de Luminy, 13288 Marseille (France). E-mail : olivier.siri@univ-amu.fr.*

[b] *Molecular Biology and Nanotechnology Laboratory (MolBNL@UniTS), Department of Engineering and Architecture (DEA), University of Trieste, 34127 Trieste, Italy. E-mail: SABRINA.PRICL@dia.units.it.*

[c] *Department of General Biophysics, University of Lodz, ul. Pomorska 141/143, Lodz 90-236, Poland*

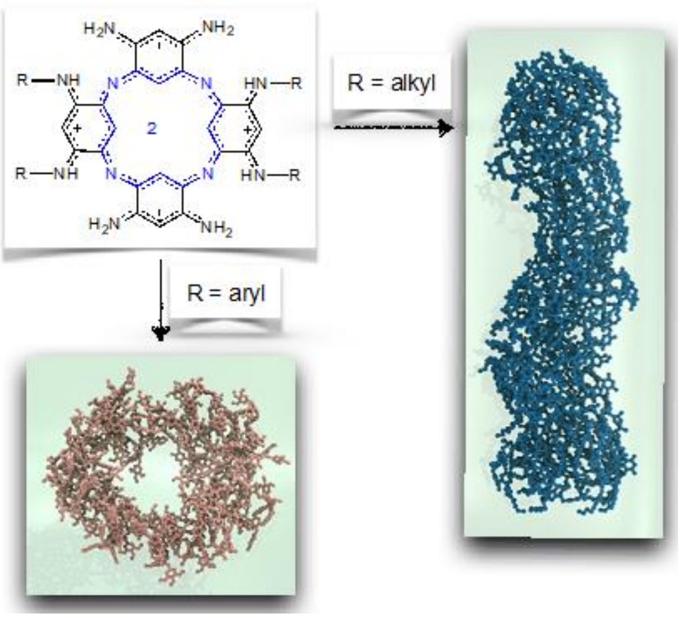

ABSTRACT: Azacalixphyrins are used as building blocks to elaborate nanostructures with different shapes depending on the nature of the N-substituents. In this work, the formation of nanoribbons from N-alkyl azacalixphyrin **4**, and of nanodonuts from the N-aryl analogue **5**, is presented and rationalized by molecular dynamics (MD) simulations. Indeed, MD revealed different modes of intermolecular interactions (defines as *nodes-and-trails* and *nodes-and-thorns* models) according to the nature of the N-substituents. Nanoribbons based on **4** results from the stackings of the azacalixphyrin cores along the vertical direction, generating the *nodes*, while the van der Waals interactions between the N-C_8H_{17} aliphatic chains generates the *trails* among the nodes along the ribbon. On the other hand, azacalixphyrin **5** self-assemblies into a nanodonut shape, in which the macrocyclic cores (*nodes*) stack along the horizontal plane while the 3,4,5-trimethoxyphenyl groups (*thorns*) point along the vertical direction towards the solvent where they establish a network of π-π interactions among their aromatic portions and H-bond interactions among the CH_3O-groups and the solvent molecules, respectively.

KEYWORDS: Azacalixphyrin, nanostructure, molecular dynamics simulations, TEM

INTRODUCTION

Azacalixphyrins of type **1** (Chart 1) recently emerged as a new class of aromatic tetraazamacrocycles [1] exhibiting unusual properties, such as a unique distribution of the π-electrons (bis-zwitterionic character), an absorption spectrum covering the whole visible region with intense absorption bands up to the NIR region (900 nm), and a very stable dianionic aromatic ring. Incorporating four C_6 rings connected by nitrogen bridges, these macrocycles can be considered as analogues of azacalixarenes **2** that brought specific properties in the calixarene family [2]. Importantly, macrocycles of type **1** feature aromaticity due to 18 π-electrons delocalized over a ring consisting of 16 atoms, with a nitrogen atom every three carbons. Thus, they belong to the porphyrinoids and can be viewed as the first "pyrrole-free" analogues of porphyrins **3** [3]. To underscore these analogies, we named these exotic macrocycles "azacalixphyrin".

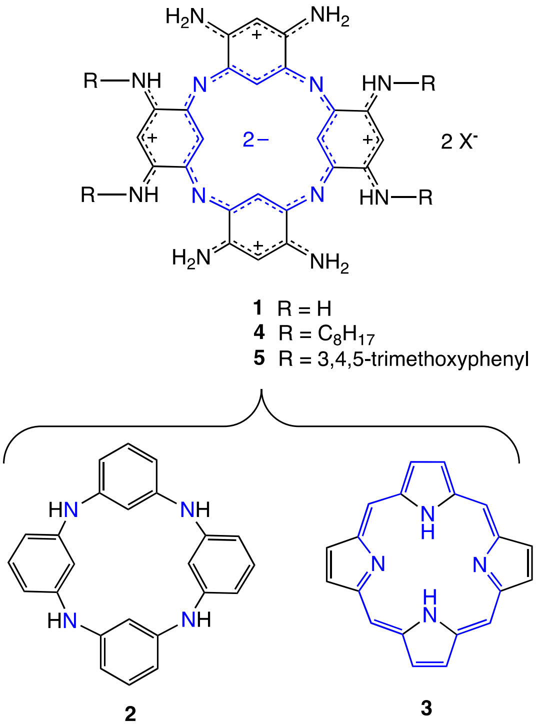

Chart 1. Azacalixphyrins at the crossroad of the azacalixarenes and the porphyrines

The first preparation of the (parent) unsubstituted azacalixphyrin macrocycle **1** was reported in two steps ten years ago highlighting the remarkable optical properties but also a very poor solubility which impedes straightforward experimental studies [1]. This limitation parallels the case of porphine in the history of porphyrins [4]. The introduction of N-substituents at the periphery (e.g., **4** and **5**), see Chart 1) allowed improving the solubility in organic solvents, and shifting the optical properties further to the NIR range [5,6,7]. The strong NIR absorption at 900 nm was then exploited to investigate N-substituted azacalixphyrins as 1) photoacoustic contrast agents to generate ultrasounds with an amplitude depending on the absorption coefficient of the dyes [6], and 2) photoinitiating agent because of its ability to promote photopolymerization on its own, avoiding the introduction of co-initiators [8]. Noteworthy, the development of a highly delocalized fused bis-azacalixphyrin was also described featuring the short wavelength infrared range beyond 1000 nm (NIR II window) [9].

In term of applications, porphyrins appeared also very attractive for decades in the construction of self-assembled nanomaterials, with well-defined shapes and dimensions, that are very useful for different technological sectors ranging from catalysis and sensing to solar energy conversion and storage [10]. In the short history of azacalixphyrins, macrocycle

4 bearing N-alkyl substituents was shown to form well-defined molecular ribbons that we assumed to be stabilized through van der Waals interactions between the chains [5]. Herein, we wish to demonstrate that the morphology of the azacalixphyrin nanostructure can be tuned by the nature of the N-substituents from nanoribbons [N-alkyl (**4**)] to nanodonuts [N-aryl (**5**)]. The characterization of the new nanostructured materials based on **5** were investigated by several microscopic techniques and a detailed molecular dynamics study that could identify the nature of the supramolecular interactions and the key role of the N-substituents.

EXPERIMENTAL

General

Nuclear Magnetic Resonance was recorded on a JEOL ECS400 NMR spectrometer at room temperature. NMR chemical shifts are given in ppm (δ) relative to Me_4Si with solvent resonances used as internal standard (CD_3OD: 3.31 ppm for ^1H and 49.0 for $^{13}C[^1H]$). UV-Vis-NIR absorption spectra were recorded on a VARIAN CARY 50 SCAN spectrophotometer at room temperature. All reagents were purchased from Sigma-Aldrich and used as received. Brockmann III activated basic aluminium oxide was prepared from Brockmann activity I Al_2O_3 mixed with 6 wt.% of water (75 mg Al_2O_3 + 4,5 mL H_2O).

Microscopy

A Jeol JSM-6320F Scanning Electron Microscope (SEM) operating at 15 kV and equipped with a secondary electron detector was used to record images at low magnification. At high magnification, images were obtained in bright field mode by a Jeol JEM-2011 Transmission Electron Microscope (TEM) equipped with a LaB_6 electron gun operating at 200keV, and assisted by the Digital Micrograph software (GATAN). ImageJ freeware (https://imagej.nih.gov/ij) was also used to measure the size of the observed solid particles.

Calculations

*Self-assembling of **4** and **5** in methanol solution by atomistic molecular dynamics simulations*. The three-dimensional molecular models of **4** and **5** were built with the AVOGADRO [11] software, and then parametrized using the gaff2 [12] forcefield *via* the *antechamber* program of the AMBER22 suite [13]. Charges for both molecules were calculated using the RED server [14]. For each system, an initial random configuration was constructed by placing 60 molecules of **4** and 40 molecules of **5** inside the respective boxes (10 x 10 x 6 nm) using PACKMOL [15]. Solvation (with methanol or water) and topology preparation was finally achieved *via* the *tleap* program of AMBER22. Next, a well validated simulation procedure based on atomistic molecular dynamics simulations was performed [16]. Briefly, electrostatic interactions were treated via the particle mesh Ewald (PME) algorithm [17], and temperature was regulated by the Langevin method [18] (with a collision frequency of 2.5 ps^{-1}). During the isothermal/isobaric MD simulations, pressure was maintained at 1 atm by the Berendsen barostat [19] during the equilibration stages, while the Monte Carlo barostat implemented in PMEMD engine of AMBER22 was used during the production stages of the simulations. The SHAKE algorithm [20] was applied to allow a 2 fs integration time step during the equilibration and production stages, while in the heating phase a 1 fs time step was adopted. Each system was initially energy minimized through a combination of steepest descent (3000 iterations) and conjugated gradient (3000 iterations) algorithms. Then, first temperature was slowly increased to 298 K in the constant-temperature/constant-volume ensemble (NVT), then MD simulations conditions were switched to the constant temperature/constant pressure (NPT) ensemble until constant density was attained, and finally the evolution and equilibration of each system into the corresponding self-assembled structure was followed during a period of 5 µs.

*Derivation of the potential of mean force for the dimerization of **4** and **5**.* To retrieve the potential of mean force (PMF) along the distance separating a dimer into either two **4** or **5** monomers, respectively, and the relevant free energy (ΔG) values, we used a well-established protocol [21] based on Umbrella Sampling (US) [22]. The path dividing the dimer into its monomers was described as a function of the distance from the center of mass (COM) of the two molecules from 0 to 2 nm in 30 equally spaced windows. The distance in each window was restrained with a force of 2.5 kcal/mol, and the data collection in each window was carried on for 5 ns after allowing for 1 ns of equilibration. The Weighted Histogram Analysis (WHAM) method [23] was then employed to retrieve the PMF along the distance between the two-molecule pair.

*Estimation of the enthalpic and entropic contribution to the dimerization of **4** and **5** in methanol solution by atomistic molecular dynamics simulations*. To estimate the enthalpic contribution (ΔH) to the formation a dimer by two molecules of either **4** or **5**, we adopted the procedure described in detail by Fenley et al. [24] according to which ΔH is the difference between the mean energies of two systems: 1) the initial state, composed of the free molecule (**4** or **5**) in the solvent and 2) the final state, composed of the dimer in the same solvent plus an amount of pure solvent that exactly balances the solvent of the initial and final states. Accordingly, the enthalpic contribution can be calculated as $\Delta H \approx \Delta U < U_{\mathrm{dimer,2N}} > - 2 < U_{\mathrm{monomer,N}} >$, in which the values enclosed by angle brackets represent the mean total potential energies of the dimer with 2N solvent molecules and the monomer with N solvent molecules, respectively. Finally, with ΔG and ΔH at hand, the entropic contribution to free energy was obtained from the fundamental thermodynamic relationship: $\Delta G = \Delta H - T\Delta S$.

Organic synthesis

Compound **4** was prepared and purified as described in the literature [6]. Compounds **5** was prepared as described [6] excepted for the reduction step of **6** which has been optimized.

Synthesis of N^2,N^4,N^{14},N^{16}-tetrakis(3,4,5-trimethoxyphenyl)-azacalixphyrin (5)

In a pressure bomb, tetrakis(3,4,5-trimethoxyphenyl)-azacalix[4]arene precursor [6] (130 mg, 102 µmol, 1 equiv.) and Pd on carbon (5 wt.% Pd/C, 65 mg, 31 µmol, 0.3 equiv.) were mixed in 60 mL of freshly distilled tetrahydrofuran. Hydrazine monohydrate (500 µL, 10.24 mmol, 100 equiv.) was added to the mixture before closing the bomb with a Teflon seal. The reaction was vigorously stirred at 80 °C for 3 days, then the solution was cooled down to room temperature, transferred in a round bottom flask equipped with a condenser and diluted with 500 mL of methanol. The mixture was stirred at 40 °C for 3 days under aerobic atmosphere, then it was filtered on a Celite plug (AW). The small plug was rinsed with methanol and the collected solution was evaporated under reduced pressure. The obtained residue was dissolved in a minimum amount of methanol, added by three spatulas of basic activated Al_2O_3 (Brockmann III) and evaporated under reduced pressure to afford a solid aluminium oxide cake containing the crude compound, which was deposited on an alumina column chromatography (basic Al_2O_3, Brockmann III activity). The column was eluted using a dichloromethane/methanol mixture, with a gradient going from 99/1 to 90/10. The fractions containing the product were identified by UV-vis-NIR absorption (λ_{max} (MeOH) = 938 nm), combined, and evaporated under reduced pressure. The obtained solid was dissolved in dichloromethane and filtered on paper to remove the potential traces of aluminium oxide that may have been solvated during the chromatography. After evaporation of the solvent and drying, the product was isolated as a dark solid in 68% yield (79 mg, 69 µmol). The ^1H NMR analysis and the electronic absorption in methanol matched the previously reported data. ^1H NMR (400 MHz, CD_3OD, 298 K): $\delta = 7.05$ (s, 2H, C(+)H), 6.79 (s, 8H, CH_{Ar}), 6.17 (s, 2H, C(+)H), 3.83 (s, 12H, OCH_3), 3.79 (s, 24H, OCH_3), -0.82 (s, 4H, C(-)H).

RESULTS AND DISCUSSION

N-aryl substituted azacalixphyrin **5** was prepared by optimising the reduction step procedure of azacalixarene **6** described in the literature (Scheme 1) [6]. The four nitro functions were reduced in presence of hydrazine monohydrate and Pd/C under heating for 72 hrs (instead of 30) at 80 °C (instead of 100 °C) to afford the corresponding colourless octaamino-azacalix[4]arene intermediate (not isolated) that spontaneously oxidize to **5** under aerobic conditions. Due to a relatively good solubility in polar organic solvents, aryl-substituted macrocycles **5** could be purified through flash column chromatography on alumina and was isolated as a green powder in 68% yield (instead of the previously reported 45% yield).

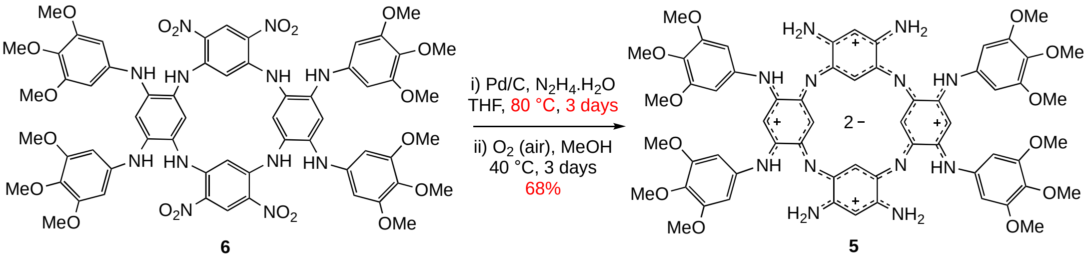

Scheme 1. Optimized synthesis of **5**

The absorption spectra of the N-substituted azacalixphyrins **4** [5] and **5** [6] in MeOH have essentially the same features compared to **1** [1], exhibiting four main bands covering the entire visible light spectrum and an additional broad and intense absorption in the NIR region (see Figure 1). Interestingly, the low energy transition is redshifted depending on the N-substituents, going from the unsubstituted parent **1** (λ_{max} = 877 nm), to the tetraalkylated molecule **4** (λ_{max} = 893 nm) and finally to the tetraaryl azacalixphyrin **5** (λ_{max} = 938 nm) (see Figure 1).

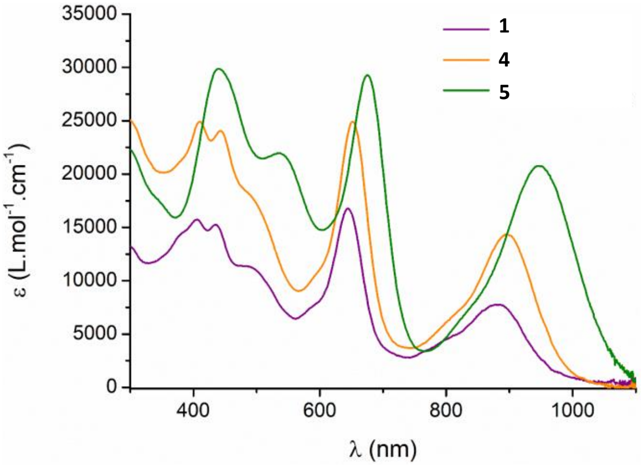

Fig. 1. Absorption profile of azacalixphyrins **1**, **4**, and **5** in MeOH.

We previously showed that **4** is able to self-assemble in MeOH into well-defined molecular ribbons (Figure 2) [5]. Investigations of **4** by transmission and scanning electron microscopy (TEM and SEM, respectively) revealed the formation of 700 nm wide ribbon-like structures that are as long as 1.0 to 1.6 mm. If several supramolecular intermolecular interactions could be envisaged, we hypothesized that the nano-structure shape might be controlled through van der Waals interactions between the N-octyl chains [5].

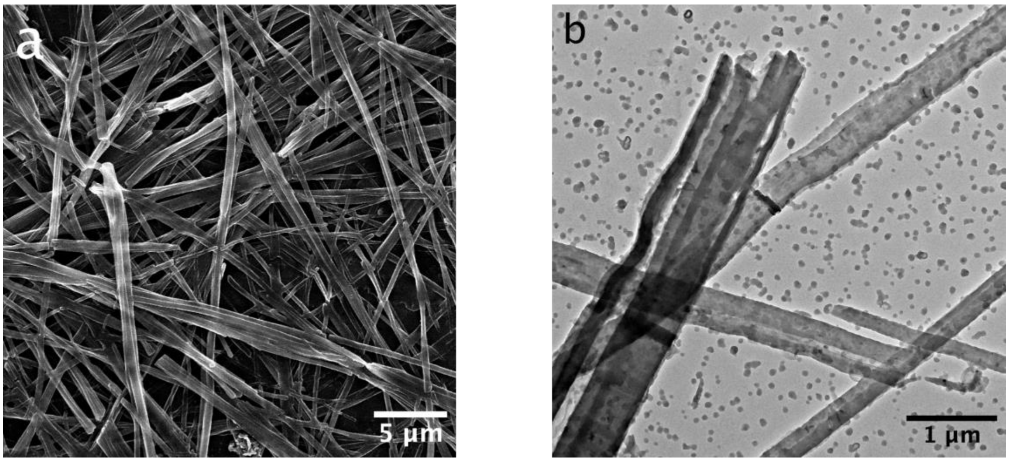

Fig. 2. SEM (a) and TEM (b) images of self-assembled **4**

Remarkably, we now observed that the morphology of the azacalixphyrin nanostructure can be tuned by the nature of the N-substituents. Indeed, introduction of N-aryl (**5**) leads in a mixture THF/H_2O (1/250) to the formation of nanodonuts of different sizes as showed in Fig 3. Note that azacalixphyrin nanodonuts are mainly aggregated although a few are isolated as illustrated in Fig 3a.

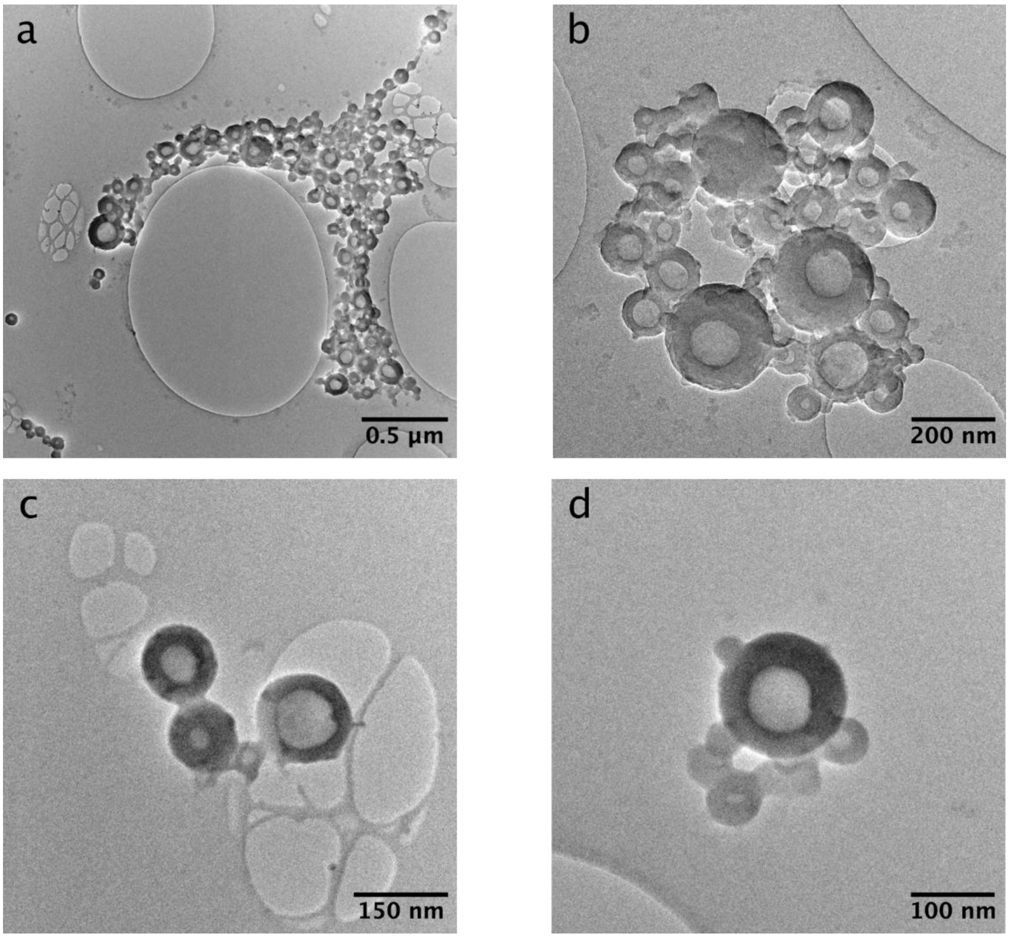

Fig. 3 a-d. Observation of azacalixphyrin nanodonuts (obtained from **5**) in TEM at increasing magnification

Measurement of the inner and outer diameters of the nanodonuts performed on the TEM images shows that their outer diameter is typically between 20 and 300 nm while the inner diameter is between 15 and 80 nm, as shown in Fig 4 for an aggregate composed of about 50 nanodonuts. It is worth mentioning that for an outer diameter of less than about 40 nm, the azacalixphyrin particles do not have an empty inner part, thus looking like circular or spherical particles. It is clearly visible in Fig.3d.

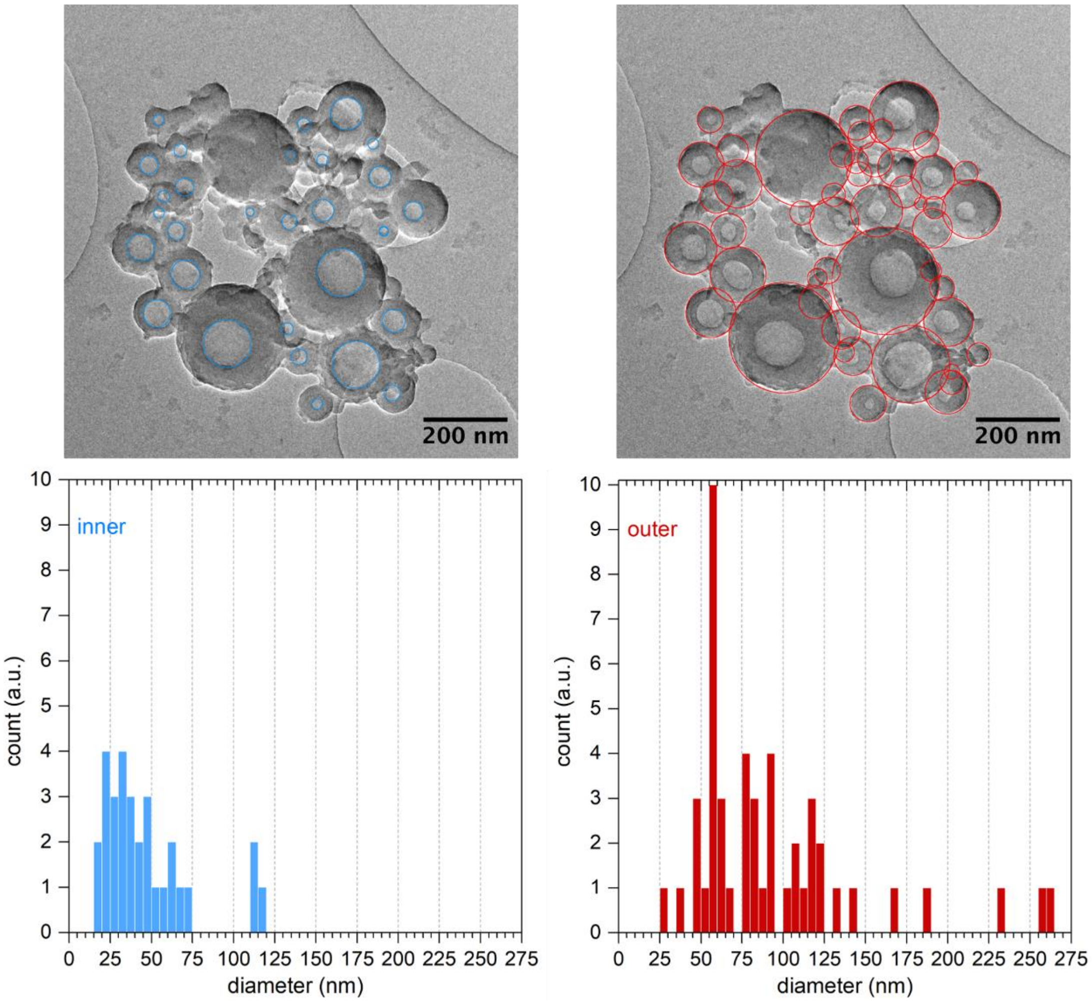

Fig. 4. (Top panel) TEM observation of aggregated nanodonuts of **5** indicating their inner (blue circle) and outer (red circle) diameter. (Bottom) Size distribution of the inner (left) and outer (right) diameter

Molecular dynamics (MD) calculations carried out on **4** and **5** were performed to gain insights into the morphology of the nanostructure (nanoribbons *vs*. nanodonuts) and the role of the N-substituents (alky *vs*. aryl). Starting from the corresponding isotropic dispersions of **4** and **5** in MeOH and water, respectively (left panels in Figure 5), the 5 μs long MD simulations indeed led to the formation of a ribbon-like structure in the former case (Figure 5, top right panel) and of a donut-like structure in the latter (Figure 5, bottom right panel).

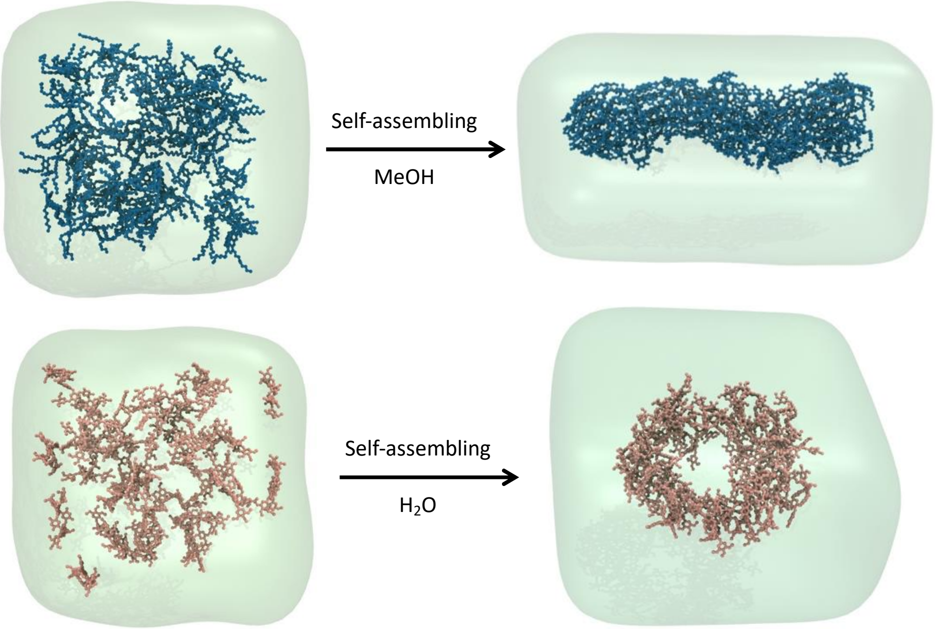

Fig. 5. (Top panel) Initial random dispersion (left) and final self-assembled ribbon-like structure of **4** (blue sticks-and-balls) in MeOH solution (light green surface) as obtained from atomistic MD simulations. (Bottom panel) Initial random dispersion (left) and final self-assembled donut-like structure of **5** (pink sticks-and-balls) in water (light green surface) as obtained from atomistic MD simulations.

As shown in detail in Figure 6, the self-assembled nanoribbon structure of **4** can be described as a *nodes-and-trails* model, in which the stackings of the azacalixphyrin cores along the vertical direction generate the *nodes* whilst the packing of the N-C_8H_{17} aliphatic chains develops along the horizontal direction through van der Waals interactions, generating the *trails* among the nodes along the ribbon.

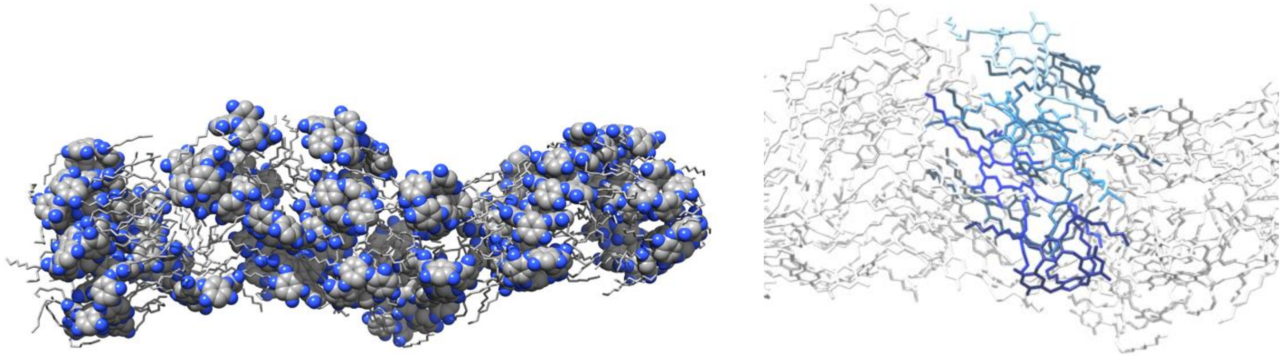

Fig. 6. (Left) Snapshot of the "nodes-and-trails" nanoribbon structure generated from the self-assembly of **4** as extracted from the equilibrated portion of the corresponding MD trajectory. The azacalixphyrin cores are depicted as atom-colored spheres (C, gray; N, blue) to highlight the *nodes* while the aliphatic chains making up the *trail* portions are shown as gray sticks. (Right) Zoom on the vertical stacking of the azacalixphyrin cores making up a *node* along the nanoribbon. The different molecules making up the selected *node* are shown in different shade of blue sticks. In both panels, hydrogen atoms and solvent molecules are omitted for clarity.

The presence of aromatic decorations in **5** drives another shape of the ultimate self-assembled structure into a *nodes-and-thorns* model (Figure 7), in which the azacalixphyrin cores stack along the horizontal plane forming the *nodes* while the CH_3-O-subsituted aromatic portions (*thorns*) point along the vertical direction towards the solvent.

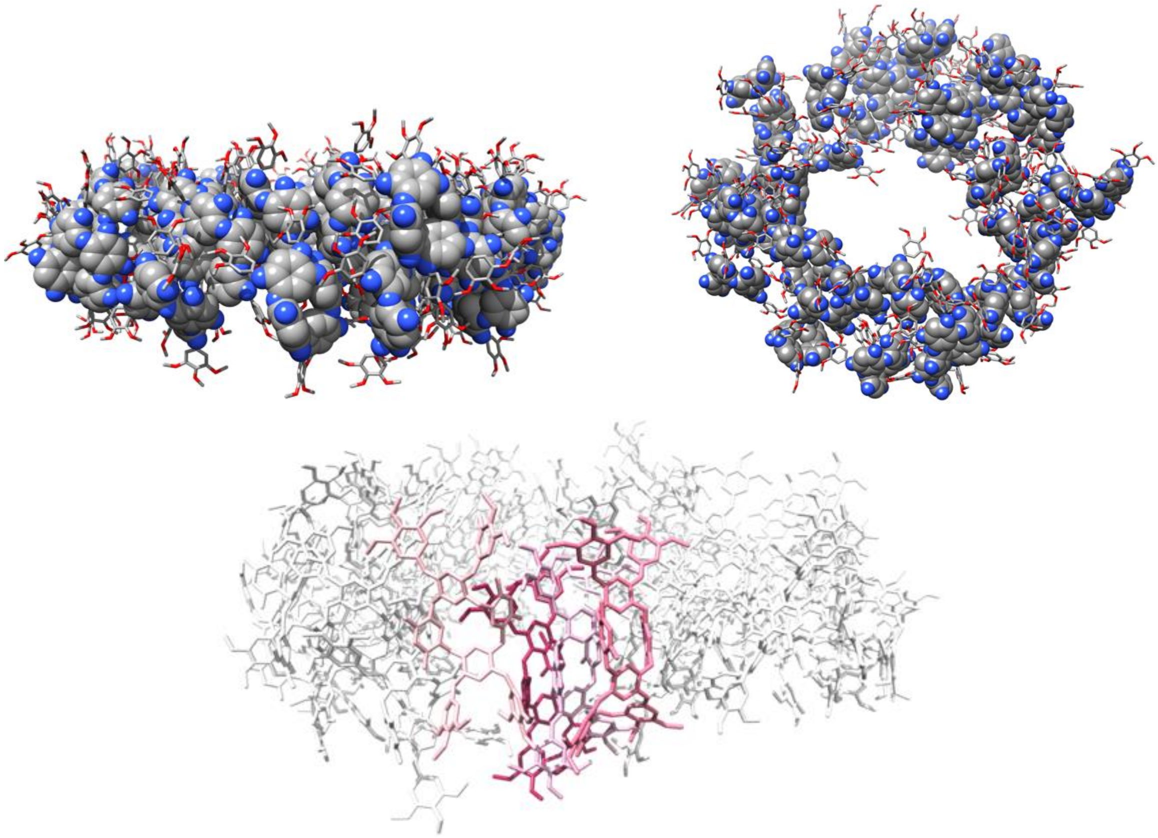

Fig. 7. (Top) Snapshots of the *nodes-and-thorns* nanodonut structure generated from the self-assembly of **5** as extracted from the equilibrated portion of the corresponding MD trajectory. The azacalixphyrin cores are depicted as atom-colored spheres (C, gray; N, blue) to highlight the *nodes* while the CH_3O-substituted aromatic rings making up the *thorn* portions are shown as atom-colored sticks (C, gray, O, red). (Bottom) Zoom on a portion of the horizontal stacking of the azacalixphyrin cores making up the *nodes* along the nanodonuts. The different molecules making up the selected *node* portion are shown in different shade of pink sticks. In all panels, hydrogen atoms and solvent molecules are omitted for clarity.

As, in principle, both **4** and **5** can provide stacking forces within the *nodes* but should differ in the contribution afforded to self-assembly by their *trail* and *thorn* components - the balance of which could be responsible for the molecular ordering and the final relevant nanomorphology - we further performed atomistic MD simulations to derive the potential of mean force (PMF) associated with the dimerization of **4** (in MeOH) and **5** (in H_2O) , respectively. The curves shown in Figure 8A reveal a similarity in the corresponding PMF profiles hinting for similar aggregation strength for the two molecules. The calculated value of the aggregation free energies (ΔG) obtained from the PMF curves and shown in Figure 8B numerically support this idea, the corresponding values being ΔG = -13.2 ± 0.6 kcal/mol in the case of **4** and ΔG = -12.7 ± 0.5 kcal/mol in the case of **5**. Additional simulations carried out separately for the dimeric and monomeric form of both molecules in solution led to the estimation of the enthalpic contribution (ΔH) to ΔG and, ultimately, to the corresponding -TΔS value *via* the fundamental thermodynamic relationship ΔG = ΔH - TΔS, as also shown in Figure 8B. As it could be somewhat expected, the nature of the interactions leading to dimer formation in both cases is prevalently enthalpic (ΔH(**4**) = -18.2 ± 1.3 kcal/mol, ΔH(**5**) = -16.1 ± 0.74 kcal/mol, respectively), whilst entropy tends to oppose aggregation by virtue of a decrease in the molecular degrees of freedom upon binding (-TΔS(**4**) = +5.05 ± 1.49 and -TΔS(**5**) = +3.38 ± 1.11 kcal/mol, Figure 8B).

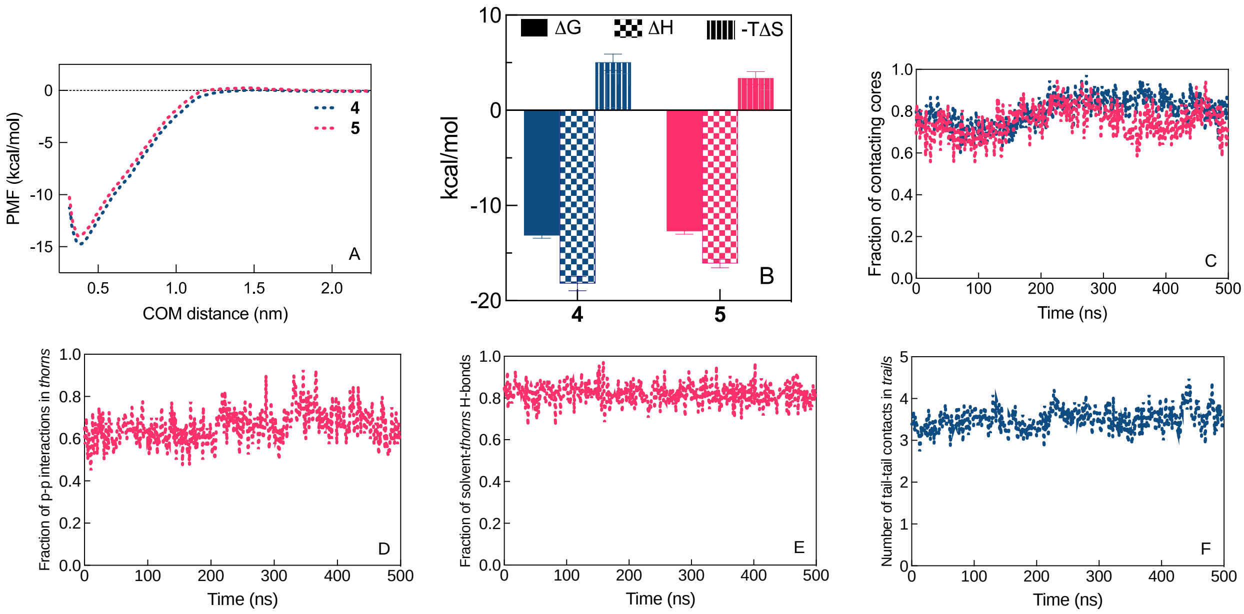

Fig. 8. (A) Potentials of mean force (PMF) for the dimerization of **4** (in MeOH) and **5** (in H_2O) at room temperature and pressure. (B) Free energy variation (ΔG) along with the corresponding enthalpic (ΔH) and entropic (-TΔS) contributions for the association of **4** and **5**. (C) Fraction of the azacalixphyrin cores involved in π-π interactions within the *nodes* during the last 0.5 μs MD simulation of the self-assembled structure of **4** (pink) and **5** (blue). (D) Fraction of the aromatic 3,4,5-trimethoxyphenyl moieties (*thorns*) that are involved in π-π interactions with other *thorns* during the MD simulation of the self-assembled structure of **5**. (E) Fraction of the CH_3-O- moieties in *thorns* involved in H-bonds with the solvent. (F) Number of tails contacted by each aliphatic chain of **4** within the *trails* during the MD simulation of the self-assembled structure of **4**.

Finally, further analysis of the terminal, equilibrated portions of the MD trajectories for the self-assembled nanoribbon and nanodonut reveals that the average fraction of the azacalixphyrin cores involved in π-π interactions within the *nodes* of the corresponding *node-and-trails* (**4**) and *nodes-and-thorns* (**5**) nanostructures is comparable (80% in the nanoribbon and 75% in the nanodonut, respectively), supporting a similar contribution of the common, central ring system in the two different supermolecular aggregates afforded by this type of stabilizing interactions (Figure 8C). Also, the average fractions of the aromatic 3,4,5-trimethoxyphenyl moieties (*thorns*) that are involved in π-π interactions with other *thorns* and H-bond interactions with the solvent through their CH_3O- groups during the MD simulation of the self-assembled structure of **5** are quite relevant (66%, Figure 8D, and 82%, Figure 8E, respectively), as is the average number of tails (3.5) contacted by each aliphatic chain of **4** within the *trails via* van der Waals and hydrophobic interaction during the MD simulation of the corresponding self-assembled structure (Figure 8F). Interestingly, in the case of the nanoribbon the slightly higher fraction of π-π stacking within the *nodes* and the high number of hydrophobic contacts within the *trails* afford the major stabilizing contribution to ΔG. This, in turn, is somewhat contrasted by the ordering of the hydrocarbon chains along the trails, resulting in the substantial decrease in system entropy discussed above which, however, is overcompensated by the favorable overall enthalpic term. For the nanodonut, the still high fraction of stacking interaction characterizing the *nodes* coupled with the density of similar contacts among the *thorns* and the relevant number of H-bonds exchanged with the solvent molecules also bring along a favorable contribution to ΔH (and hence to ΔG), although to a slightly lower extent than that predicted in the case of the nanoribbon (Figure 8B). Contextually, the more rigid aromatic moieties of **4** undergo a lesser penalty upon interacting among each other with respect to the flexible aliphatic chains of **5** and this, ultimately, results in comparable, favorable ΔG values for both the nanoribbon by **4** and the nanodonut by **5**. In short, the main distinctive driving force leading to self-assembly for **4** is based on hydrophobic and van der Waals interactions between the hydrocarbon chains that, by organizing into trails, minimize their contact with the solvent environment. In the case of molecule **5**, while the π-π stackings among the azacalixphyrin cores are somewhat like those seen for **4**, the occurrence of small aromatic rings characterized by the presence of two hydrophilic CH_3O- groups leads these molecules to expose such substituents to the solvated environment where they form an extensive network of hydrogen bonds.

CONCLUSION

Azacalixphyrins can be used as a promising platform to build nanostructures with different shapes depending on the nature of the N-substituents. Indeed, in this work the formation of nanoribbons or nanodonuts could be indeed observed from N-alkyl (**4**) to N-aryl (**5**) azacalixphyrins, respectively. To the best of our knowledge, the access to nanodonuts based on **5** differs from those described in the literature which are generated from other types of building blocks [25-28]. Molecular dynamics simulations revealed that self-assembled nanoribbon structure based on **4** could be described in terms of a *nodes-and-trails* model, in which the stackings of the azacalixphyrin *cores* along the vertical direction, generating the *nodes*, while the packing of the N-C_8H_{17} aliphatic chains (mainly driven by hydrophobic and van der Waals interactions) develops along the horizontal direction, generating the *trails* among the *nodes* along the ribbon. For the nanodonuts, the N-aryl substituents led to another shape of the self-assembled nanostructure into a *nodes-and-thorns* model in which the azacalixphyrin cores stack along the horizontal plane forming (*nodes*) while the methoxy groups (OMe) (*thorns*) point along the vertical direction towards the solvent and are stabilized by a plethora of π-π interactions among the thorns and solvent-mediated H-bonds. This controlled versatility paves the way to the elaboration of nanomaterials with pre-defined shape tuned by chemical engineering at the molecular level. More specifically, the formation of such nanoassemblies in protic solvents (including in water) might be investigated to prepare new nanovectors for biology.

Acknowledgements

This work was supported by the Centre National de la Recherche Scientifique, the Ministère de la Recherche et des Nouvelles Technologies (France). SP and DM acknowledge access to supercomputing resources and financial support from ICSC – Centro Nazionale di Ricerca in High Performance Computing, Big Data and Quantum Computing (Spoke 7, WP5 (Materials Foundry), Task T.2 Development of computational workflows based on atomistic molecular simulations for the prediction of key properties of molecular system and high-performance (nano)materials for biological, pharmaceutical and industrial application)– and CINECA, funded by European Union – NextGenerationEU.

REFERENCES

1. Chen Z., Giorgi M., Jacquemin D., Elhabiri M., Siri O. *Angew. Chem. Int. Ed.* 2013; **52**: 6250.
2. a) Tsue H., Ishibashi K., Tamura R., *Top. Heterocycl. Chem.* 2008; **17**: 73–96; b) Wang M.-X. *Chem. Commun.* 2008; 4541–4551; c) Wang, M.-X. *Acc. Chem. Res.* 2011; **44**: 182–195. d) Tsue H., Ishibashi K., Tokita S., Takahashi H., Matsui K., Tamura R. *Chem. Eur. J.* 2008; **14**: 6125–6134; e) Konishi H., Hashimoto S., Sakakibara T., Matsubara S., Yasukawa Y., Morikawa O., Kobayashi K. *Tetrahedron Lett.* 2009; **50**: 620–623; f) Haddoub, R. Touil M., Chen Z., Raimundo J.-M., Marsal P., Elhabiri M., Siri O. *Eur. J. Org. Chem.* 2014; 745–752; g) Katz J. L., Tschaen B. A. *Org. Lett.* 2010; **12**: 4300–4303.

3. a) Kadish K. M., Smith K. M., Guilard R. *Handbook of Porphyrin Science: With Applications to Chemistry, Physics, Materials Science Engineering, Biology and Medicine (Ed.:)*, World Scientific Press, Singapore, 2011. b) Vinodh M., Alipour F. H., Mohamod A. A., Al-Azemi T. F. *Molecules* 2012; 17: 11763–11799. c) Li L. L., Diau E.W.-G. *Chem. Soc. Rev.* 2013; **42**: 291–304
4. a) Neya S., Yodo H., Funasaki N. *J. Hetero. Chem.* 1993; **30**: 549-550. b) Neya S., Quan J., Hata M., Hoshino T., Funasaki N. *Tetrahedron Lett.* 2006; **47**: 8731-8732.
5. Chen Z., Haddoub R., Mahe´ J., Marchand G., Jacquemin D., Andeme Edzang J., Canard G., Ferry D., Grauby O., Ranguis A., Siri O. *Chem. – Eur. J.* 2016; **22**: 17820.
6. Lavaud L., Pascal S., Metwally K., Gasteau D., Da Silva A., Chen Z., Elhabiri M., Canard G., Jacquemin D., Siri O. *Chem. Commun.* 2018; **54**: 12365.
7. Lavaud L., Azarias C., Canard G., Pascal S., Jacquemin D., Siri O. *New J. Chem.* 2020; **44**: 18130-18137.
8. Breloy L., Mhanna R., Malval J.-P., Brezová V., Jacquemin D., Pascal S., Siri, O., Versace D.-L. *Chem. Commun.* 2021; **57**: 8973-8976.
9. Lavaud L., Azarias C., Canard G., Pascal S., Galiana J., Giorgi M., Chen Z., Jacquemin D., Siri O. *Chem. Commun*. 2020; **56**: 896-899
10. a) La D., Ngo H. H., Nguyen D. D., Tran N. T., Vo H. T., X. Nguyen H., Woong Chang S., Chung W. J., Nguyen M. B. *Coord. Chem. Rev.* 2022; **463**: 214543. b) Wang D., Niu L., Qiao Z.-Y., Cheng D.-B., Wang J., Zhong Y., Bai F., Wang H., Fan H. *ACS Nano* 2018; **12**: 3796–3803.
11. Hanwell M. D., Curtis D. E., Lonie D. C., Vandermeersch T., Zurek E., Hutchison G. R. *J. Cheminf.* 2012; **4**: 1–17.
12. Junmei W., Romain M. W., James W. C., Peter A. K., David A. C. *J Comput Chem* 2004; **25**: 1157-1174.
13. Case D. A., Aktulga H. M., Belfon K., Ben-Shalom I. Y., Berryman J. T., Brozell S. R., Cerutti D. S., Cheatham III T. E., Cisneros G. A., Cruzeiro V. W. D., Darden T. A., Duke R. E., Giambasu G., Gilson M. K., Gohlke H., Goetz A. W., Harris R., Izadi S., Izmailov S. A., Kasavajhala K., Kaymak M. C., King E., Kovalenko A., Kurtzman T., Lee T. S., LeGrand S., Li P., Lin C., Liu J., Luchko T., Luo R., Machado M., Man V., Manathunga M., Merz K. M., Miao Y., Mikhailovskii O., Monard G., Nguyen H., O'Hearn K. A., Onufriev A., Pan F., Pantano S., Qi R., Rahnamoun A., Roe D. R., Roitberg A., Sagui C., Schott-Verdugo S., Shajan A., Shen J., Simmerling C. L., Skrynnikov N. R., Smith J., Swails J., Walker R. C., Wang J., Wang J., Wei H., Wolf R. M., Wu X., Xiong Y., Xue Y., York D. M., Zhao S., Kollman P. A., AMBER 2022. *University of California, San Francisco* **2022**.
14. Vanquelef E., Simon S., Marquant G., Garcia E., Klimerak G., Delepine J. C., Cieplak P., Dupradeau F.-Y. *Nucleic Acids Res.* 2011; **39**: W511–W517.
15. Schott-Verdugo S., Gohlke, H. *J Chem Inf Model* 2019; **59**: 2522-2528.
16. Ding L., Lyu Z., Tintaru A., Laurini E., Marson D., Louis B., Bouhlel A., Balasse L., Fernandez S., Garrigue P., Mas E., Giorgio S., Pricl S., Guillet B., Peng L. *Chem Commun* 2019; **56**: 301-304.
17. Toukmaji A., Sagui C., Board J., Darden T. *J. Chem. Phys.* 2000; **113**: 10913–10927.
18. Loncharich R. J., Brooks B. R., Pastor R. W. *Biopolymers* 1992; **32**: 523–535.
19. Berendsen H. J. C., Postma J. P. M., van Gunsteren W. F., DiNola A., Haak J. R. *J Chem Phys* 1984; **81**: 3684-3690.
20. Ryckaert J.-P., Ciccotti G., Berendsen H. J. C. *J Comput Phys* 1977; **23**: 327-341.
21. Marson D., Laurini E., Fermeglia M., Smith D. K., Pricl, S. *Fluid Phase Equilibr* 2018; **470**: 259-267.
22. Maria M., Ioan A. *J Chem Phys* 2008; **129**, 114101.
23. Kumar S., Rosenberg J. M., Bouzida D., Swendsen R. H., Kollman P. A. *J. Comput. Chem.* 1992; **13**: 1011–1021.
24. Fenley A. T., Henriksen N. M., Muddana H. S., Gilson M. K. Bridging *J. Chem. Theor. Comput*. 2014; **10**: 4069-4078.

25. Khoe U, Yang Y, Zhang S. *Langmuir* 2009; **25**: 4111-4114.

26. Miras H. N., Cooper G. J. T., Long D.-L., Bögge H., Müller A., Streb C., Cronin L. *Science* 2010; **327**: 72-74.

27. Djalali R., Samson J., Matsui H. *J. Am. Chem. Soc.* 2004; **126**: 7935–7939.

28. Schreiber A., Zaitseva E., Thomann Y., Thomann R., Dengjel J., Hanselmann R., Schiller S. M. *Soft Matter* 2011; **7**: 2875-2878.